文章编号：1001-9014(XXXX)XX-0001-10

DOI:10.11972/j.issn.1001-9014.XXXX.XX.001

Peak Separation and Small-Signal Modeling Analysis of Abnormal Shift in the transconductance curve in InAs Composite Channel HEMT

GONG Yong-Heng[1,2], CHEN Yu-Xuan[1,2], SHI Jing-Yuan[1], ZHANG Da-Yong[1], SU Yong-Bo[1], DING Wu-Chang[1], DING Peng[1], JIN Zhi[1,2]

(1. High-Frequency High-Voltage Device and Integrated Circuits Center, Institute of Microelectronics, Chinese Academy of Sciences, Beijing 100029, China;
2. University of Chinese Academy of Sciences, Beijing 100049, China)

Abstract: In this work, 100 nm gate-length InP-based high electron mobility transistors (HEMTs) with a composite InGaAs/InAs/InGaAs channel are fabricated. DC measurements indicate that the InAs channel enhances transconductance but shifts the peak point toward lower V_{gs} under high V_{ds} bias. Peak separation analysis reveals the DC transconductance curve is composed of two components: the gate-controlled transconductance and the impact-ionization-induced additional transconductance. Further analysis demonstrates that the anomalous shift originates from channel impact ionization intensity variation, which is caused by changes in the gate-drain electric field rather than carrier density in the channel. Two additional current sources were introduced in the small-signal model to characterize the impact-ionization-induced transconductance, and the numerical variation trends of their parameters are consistent with the peak separation results, which validates the mechanism´s correctness. RF measurements confirm that the DC transconductance enhancement does not effectively improve RF characteristics, which is attributed to the ionization-induced transconductance having a time constant significantly larger than that of conventional transconductance components. These findings provide a theoretical foundation for controlling impact-ionization and improving effective transconductance, ultimately optimizing InAs channel HEMT design.

Key words: HEMTs, InAs, peak separation, impact ionization, transconductance, small-signal equivalent model
PACS:

对InAs复合沟道HEMT中跨导曲线异常偏移的峰分离和小信号模型分析

巩永恒[1,2], 陈宇轩[1,2], 史劲元[1], 张大勇[1], 苏永波[1], 丁武昌[1], 丁 芃[1], 金 智[1,2]

(1. 中国科学院微电子研究所 高频高压器件与集成电路研究中心, 北京 100029;
2. 中国科学院大学, 北京 100049)

摘要：本文成功制备了栅长为100 nm、具有InGaAs/InAs/InGaAs复合沟道的磷化铟基高电子迁移率晶体管(InP HEMTs)。直流测试表明，InAs沟道层的引入提升了跨导，但导致跨导峰值点在高漏压(V_{ds})偏置下向低栅压(V_{gs})方向偏移。通过峰分离分析，发现直流跨导曲线由两部分构成：栅压调控的本征跨导和碰撞电离诱导的附加跨导。进一步研究表明，该异常偏移源于沟道碰撞电离强度的变化，而这种变化主要由栅漏电场改变引起，而非沟道载流子浓度的变化。小信号模型中引入的两个额外电流源表征碰撞电离跨导，其数值变化趋势与峰分离结果的一致性验证了机理的正确性。射频测试证实，尽管直流跨导有所提升，但由于碰撞电离跨导的时间常数远大于一般跨导的时间常数，器件射频特性未能得到有效改善。这些发现为抑制碰撞电离效应及提升有效跨导提供了理论基础，对优化InAs沟道HEMT设计具有重要指导意义。

关 键 词：高电子迁移率晶体管；砷化铟；峰分离；碰撞电离；跨导；小信号等效模型
中图分类号：TN385　　**文献标识码**：A

Foundation items: Supported by The National Natural Science Foundation of China (62474195)
Biography: Gong yongheng (1997. 5-), male, Sichuan China, Ph. D. Research area involves InP HEMT and MMIC. E-mail: 472231075@qq.com;
* **Corresponding author**: E-mail: jinzhi@ime.ac.cn

Introduction

The low-noise, high-frequency and high-gain performance characteristics make InP-based high electron mobility transistors (HEMTs) considered to be one of the most competitive semiconductor devices for millimeter and terahertz monolithic integrated circuits. [1] In 2007, R. Lai et al. reported a sub-50-nm device with a maximum oscillation frequency (f_{max}) exceeding 1 THz for the first time in InP-based HEMTs. [2] In 2015, X. B. Mei et al. implemented an amplifier operating at 1 THz using a 10 stage structure based on a 25 nm InP HEMT, with a gain of 9 dB. [3] This represents the single-chip amplifier circuit with the highest operating frequency reported so far.

Introducing InGaAs with high-In composition or InAs material into the channel has been proven to significantly improve device performance due to its higher carrier mobility and saturation velocity. In 2018, Jo et al. reported an $In_{0.8}Ga_{0.2}As$ HEMT with a maximum transconductance (g_{m_max}) of 3000 mS/mm, which achieves high performance of large gate length (L_g = 87 nm) devices and represents the best performing device of the same size. [4] In 2021, Samouni et al. reported a 75-nm L_g InAs channel HEMT with a maximum transconductance of 1331 mS, achieving cutoff frequency (f_T) of 260 GHz and f_{max} of 800 GHz. [5] W. S. Park et al. obtained an InP-based HEMT with a gate length of 20 nm in 2022. The f_T of the device has been increased to 750 GHz, breaking the record of InP HEMT devices, and the f_{max} has reached 1.1 THz. [6] However, smaller bandgap also makes the device more susceptible to channel impact ionization, leading to the occurrence of kink effect. The devices reported above all exhibit the kink effect, and this phenomenon is even more remarkable in InAs/AlSb-structured HEMT devices. [7] In 2007, Chia et al. discovered that the transconductance increases rapidly when the drain voltage (V_{ds}) ≥ 0.6 V, and the peak transconductance shifts towards smaller gate voltage (V_{gs}) as the drain voltage increases in their InAs channel HEMTs. Finally they obtained f_T = 310 GHz and f_{max} = 330 GHz results under V_{ds} = 0.7 V conditions. [8] However, they lacked mechanistic analysis of the transconductance shift, but instead focused on seeking the optimal bias point to obtain better characteristics.

In this paper, we present the DC and RF characteristics of the composite InGaAs/InAs/InGaAs channel HEMTs. DC measurements show introducing InAs to the channel significantly increases transconductance but exhibits an abnormal "leftward shift" as reported in [8], which we attribute to impact ionization. The measured S parameters enable us to develop a small-signal model. Results demonstrate that the time constant of impact-ionization-induced transconductance (τ_{ii}) significantly exceeds that of conventional gate-controlled transconductance (τ_{gs}), indicating that impact ionization can not respond to high-frequency signals. RF characteristics further prove the high transconductance obtained in DC measurements fails to translate into RF performance improvement.

1 Device Fabrication

The schematic cross-section of InP-based HEMTs is shown in Fig. 1. The epitaxial layers of the devices were grown by Gas Source Molecular Beam Epitaxy (GSMBE) on 3 inch semi-insulating InP (100) substrates. From bottom to top, the layers consist of an InP substrate, a 500-nm-thick $In_{0.52}Al_{0.48}As$ buffer layer, 10-nm-thick composite channel layer which contains a 3-nm-thick $In_{0.53}Ga_{0.47}As$ layer, a 5-nm-thick InAs layer, and another 2-nm-thick $In_{0.53}Ga_{0.47}As$ layer, then a 3-nm-thick $In_{0.52}Al_{0.48}As$ spacer layer, a δ-doping plane with a concentration of $5 \times 10^{12}\,cm^{-2}$, 12-nm-thick $In_{0.52}Al_{0.48}As$ barrier layer, and a Si-Doped $In_{0.65}Ga_{0.35}As/In_{0.53}Ga_{0.47}As/In_{0.52}Al_{0.48}As$ (10/15/15 nm) composite capping layer.

The InP HEMT fabrication processes are similar to our previously reported devices. [9] The only difference is that the SiO_2 hard mask on the surface of the device was not removed. The distance between source and drain electrodes was designed as 2.4 μm. The gate metal is in the middle of the gate recess, and the length of the T-gate is 100 nm, as shown in Fig. 2(a).

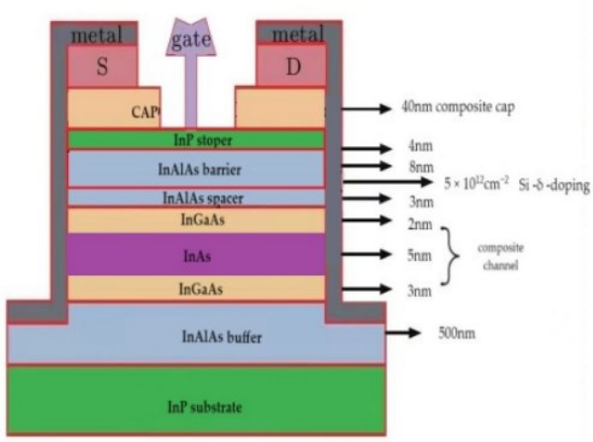

Fig. 1 schematic cross-section of InP-based HEMTs
图1 InP基HEMT横截面示意图

2 Results and Discussion

The DC and RF characteristics of InGaAs/InAs/InGaAs HEMTs were characterized by HP4142 semiconductor parameter analyzer and Agilent E8363B PNA vector network analyzer from 1 to 40 GHz under room-temperature conditions, as shown in Fig. 2(b).

A DC characteristics

Fig. 3 shows the drain current-voltage (I_d-V_{ds}) curves of the composite channel HEMT. The device has a T-shaped gate width of 2×20 μm, and the drain current in the figure has been normalized to units of mA/mm. V_{gs} is scanned from -1.5 V to 0.2 V in steps of 0.05 V, achieving a maximum drain current density (I_{d_max}) of 925.8 mA/mm, which is achieved at V_{ds} =1 V and V_{gs} = 0.2 V. (The curve family ascends from bottom to top with V_{gs} increasing from -1.5 V to 0.2 V.) In our devic-

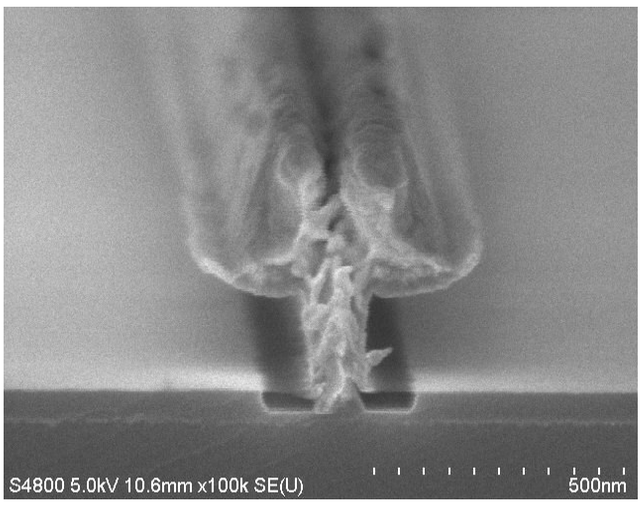

(a)

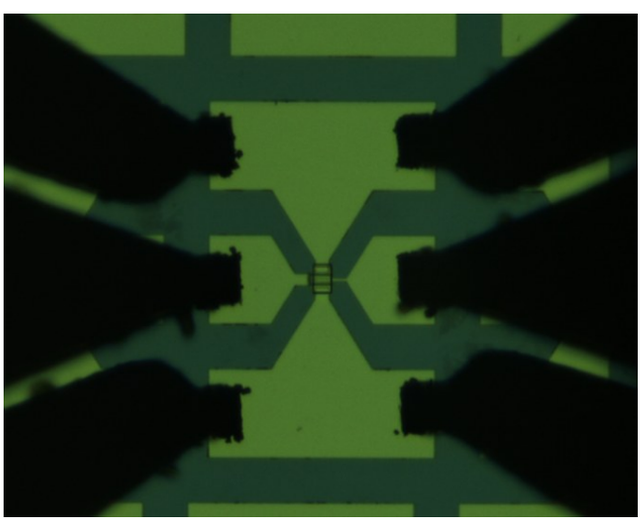

(b)

Fig. 2 Fabrication and testing characterization of T-shaped gate HEMT devices with 100 nm gate length. (a)SEM image of the T-Gate HEMTs, and (b)In situ electrical testing photograph of the T-gate HEMTs.
图2 栅长为100 nm的T型栅HEMT器件制备与测试表征(a)HEMT器件的T型栅SEM照片及(b)现场测试照片

es, the drain current does not exhibit saturation behavior with increasing V_{ds}. When V_{ds} reaches approximately 0.6 V, the output characteristic curve demonstrates significantly enhanced upward curvature compared to lower V_{ds} bias regimes, with this slope variation being more pronounced at lower V_{gs} levels.

When V_{ds} is high, the device operates in the saturation region where the current ideally should remain constant with further V_{ds} increase. However, the intensified electric field accelerates hot electrons to surmount the potential barrier into the buffer layer, generating additional current superimposed on the channel current. This phenomenon is quantified by the output conductance (g_{ds}). The kink effect refers to an abrupt drain current surge occurring beyond specific V_{ds} thresholds, deviating from the predicted saturation behavior. InAs channel devices usually suffer from serious kink effect, which is generally considered to be the result of the combined effect of surface states and channel impact ionization.[10] The characteristics in Fig. 3 align with these mechanisms, where the excess I_d enhancement arises from the combined contributions of g_{ds} and kink effects.

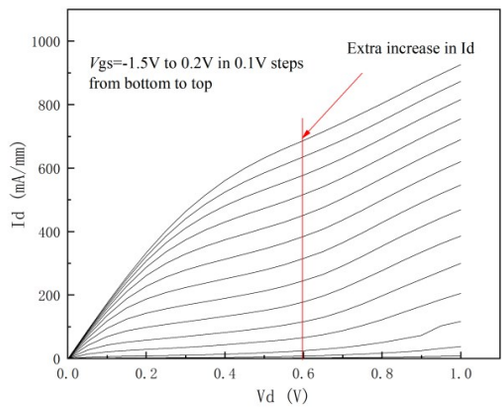

Fig. 3 Output characteristics of composite channel HEMT.
图3 复合沟道HEMT输出特性曲线

Besides the upward curvature of the output characteristic curves, gate leakage current is more frequently employed to characterize impact ionization. Fig. 4 shows the gate leakage current versus V_{ds} from 0.5 V to 1 V with 0.1 V steps. (Curves are ordered from top to bottom with ascending V_{ds} values from 0.5 V to 1 V, where the critical point at V_{ds} = 0.7 V is highlighted by a red line.) When $V_{ds} \leqslant 0.6$ V, the gate leakage profile maintains consistency with conventional Schottky junction leakage behavior. Once V_{ds} reaches 0.7 V, however, the curve develops a distinct bell-shaped (or inverted U-shaped) characteristic.

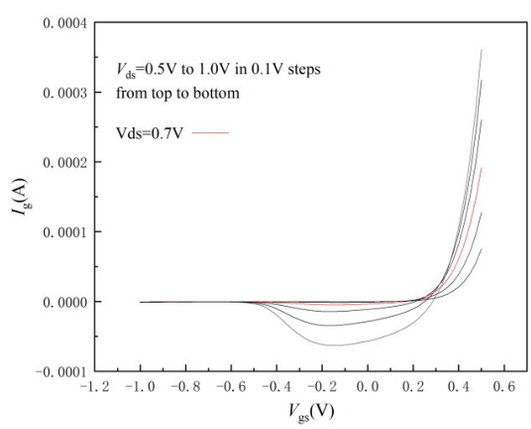

Fig. 4 The gate leakage current of the device.
图4 器件的栅极漏电流

The impact ionization intensity correlates with the gate-drain electric field strength. In the gate leakage current curves, as V_{gs} decreases from positive bias, the gate-drain potential difference (V_{dg}) progressively increases. When V_{dg} exceeds the critical threshold required for impact ionization initiation, holes injected into the gate constitute additional leakage current. With further V_{gs} reduction, despite sustained strong electric fields, the two-dimensional electron gas (2DEG) in the channel becomes depleted, ceasing electron-hole pair generation through ionization. Consequently, the gate leakage current decreases and realigns with conventional Schottky junction behavior. [11] This mechanism explains the bell-shaped profile observed in Fig. 4, confirming impact ionization occurrence.

This analysis further elucidates the enhanced upward curvature in Fig. 3 under low V_{gs} conditions at V_{ds} = 0.6 V: reduced V_{gs} elevates V_{dg}, thereby intensifying the gate-drain field and amplifying ionization effects. These observations conclusively demonstrate impact ionization activation in high V_{ds} regimes.

Fig. 5 presents the device's transfer characteristics with V_{gs} swept from -1 V to 0.5 V and V_{ds} incremented from 0 V to 1 V in 0.1 V steps. (Curves are arranged from bottom to top with V_{ds} ascending from 0 V to 1 V.) The maximum transconductance value of 1835 mS/mm is obtained at V_{ds} = 1 V and V_{gs} = -0.3 V. It is worth noting that the transconductance peak position exhibits V_{ds}-dependent behavior: for $V_{ds} \geqslant 0.5$ V, the V_{gs} corresponding to the peak transconductance no longer increases with V_{ds} as it does at low V_{ds}, but instead decreases gradually. This anomalous shift manifests as progressive leftward displacement of transconductance curve clusters under high V_{ds} conditions.

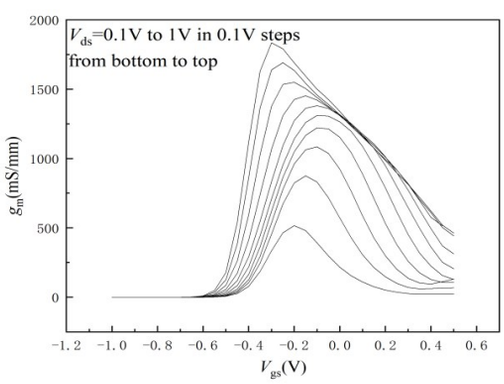

Fig. 5 The transfer characteristic curve of the device.
图5 器件的转移特性曲线

Zhong et al. explained the variation with bias of the transconductance curves in conventional HEMT devices in [12]: the transconductance of the device gradually increases with the increase of V_{ds}, and the V_{gs} corresponding to its maximum transconductance also increases accordingly; the entire curve shows a "rightward shift" trend. This rightward displacement diminishes gradually with further V_{ds} increase and ultimately stabilizes beyond specific bias thresholds, where the V_{gs} corresponding to its maximum transconductance becomes voltage-independent. Obviously, the curve clusters in Fig. 5 exhibit significant anomalies compared to those mentioned in [12].

From a functional perspective, the transconductance curve cluster can be viewed as a series of asymmetric peak functions. Under low V_{ds} bias conditions, the fitting function can characterize the asymmetry of the g_m curve by using the bi-Gaussian function as:

$$y = y_0 + He^{-0.5\left(\frac{x-x_c}{w_1}\right)^2} \quad (x < x_c) \tag{1}$$

$$y = y_0 + He^{-0.5\left(\frac{x-x_c}{w_2}\right)^2} \quad (x > x_c) \tag{2}$$

However, when $V_{ds} \geqslant 0.6$ V, the curve significantly deviates from a single bi-Gaussian peak shape, introducing substantial fitting residuals. The peak amplitude intensifies with concomitant leftward displacement, accompanied by measurable variations in full width at half maximum (FWHM). Although no distinct secondary peak appears in the overall curve, these features necessitate the introduction of a second peak function under high V_{ds} bias condition.

In HEMT devices, the channel current is controlled by the Schottky gate, while impact ionization introduces parasitic current components. According to the derivative relationship between I_d and g_m, this inevitably generates parasitic transconductance contributions. Therefore, when impact-ionization occurs, the total transconductance inherently comprises the superposition of both components; through the peak analysis of the curves, we can characterize them separately by peak separation.

Taking the transconductance curves under the condition of V_{ds}= 1 V as an example, we fit the curve with the bi-Gaussian function, and then divide it into two curves as shown in Fig. 6. The two separated curves are also characterized using Equations (1~2). Through this approach, we separate the transconductance curve cluster into two clusters to explain the performance of these two clusters of curves under different biases respectively, as shown in Fig. 7(a) and (b):

In Fig. 7(a) and (b), the transconductance curves are arranged from bottom to top in the order of progressively increasing drain-source voltage. All fitted curves exhibit determination coefficients (R^2) exceeding 0.99, indicating a good degree of fitting. Fig. 8 shows the variation of V_{gs} corresponding to g_{m_max} with V_{ds} for both transconductance components, which provides a more detailed depiction of the different shift trends shown in Fig. 7(a) and (b). As shown in Fig. 7(a) and Fig. 8, when $V_{ds} \leqslant 0.5$ V, there is no left shift in the measured transconductance curve, thus it can be considered that the measured g_m is well controlled by gate voltage; the trend of the entire curve cluster remains consistent with that mentioned in [12]. When $V_{ds} \geqslant 0.6$ V, impact ionization brings additional parasitic transconductance, manifesting as progressive peak left-shifting. Through peak separating, it can be inferred that the abnormal left shift of

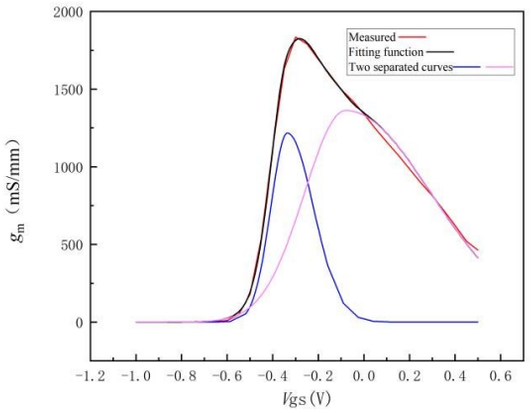

Fig. 6 Transfer characteristic curve with its fitting function curve and the two separated curves at V_{ds}= 1.0 V.
图6 Vds= 1.0 V时的转移特性曲线及其拟合曲线以及两条分离曲线

the measured transconductance curve is due to the impact ionization.

From the perspective of device physics, impact ionization intensity depends on the number of carriers entering the channel and the probability of carrier impact-ionization within the channel. The former is controlled by the gate voltage V_{gs}. Before the δ-doped carriers fully enter the channel, it can be modeled as:

$$Q_n = Q(V_{gs}) = C_0(V_{gs} - V_{th}) \tag{3}$$

Here, Q_n denotes the gate-induced channel charge, which is capacitively coupled and characterized by capacitance C_0; V_{th} is the threshold voltage, L the channel length, and μ_n the carrier mobility. For devices operating in the saturation region, the gate controlled current and corresponding transconductance are governed by:

$$I_{dsat} = \frac{Z}{L}\int_0^L Q_n(x)v(x)dx = \frac{Z\mu_n C_0}{2L}(V_{gs} - V_{th})^2 \tag{4}$$

$$g_m = \frac{Z\mu_n C_0}{L}(V_{gs} - V_{th}) \tag{5}$$

At this stage, g_m and V_{gs} exhibit a linear relationship. After the δ-doped carriers enter the channel completely, Q_n remains a constant and the channel current no longer increases with V_{gs}, g_m progressively diminishes to 0. Fig. 7(a) demonstrates that under $V_{ds} \geqslant 0.6$ V conditions, the linear g_m-V_{gs} relationship persists until V_{gs} approaches -0.1 V. This also means that the linear relationship between Q_n and V_{gs} proposed in Equation (3) has not changed.

In Fig. 7(b), the transconductance induced by impact ionization exhibits a characteristic rise-fall profile with increasing V_{gs}, while its mechanism is similar to the previous explanation of bell-shaped leakage current: the initial enhancement is due to the growth of 2DEG and the decrease is due to reduced V_{dg}. When $V_{gs} \leqslant$ -0.1 V, Q_n and V_{gs} maintain a linear relationship. Considering that the current generated by impact ionization is determined by the carriers entering the channel and their ionization

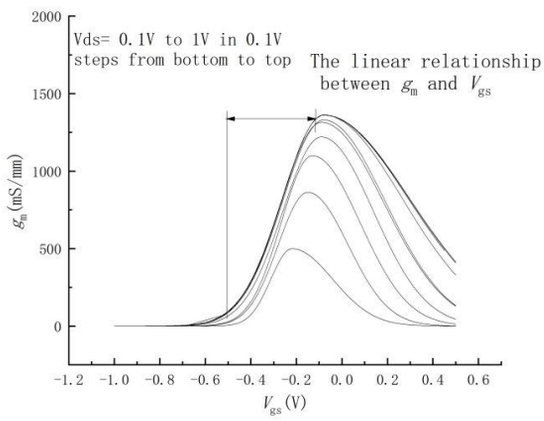

(a)

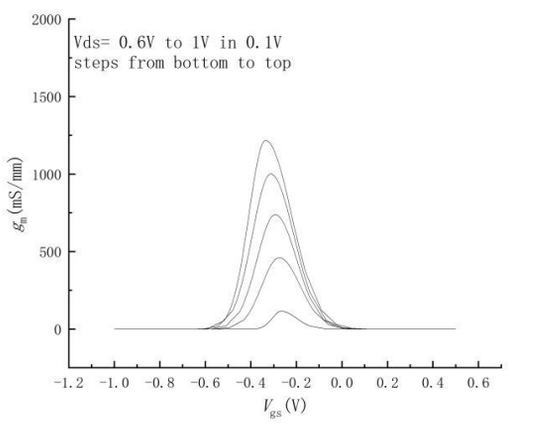

(b)

Fig. 7 Decomposition of DC transconductance curves via peak separation. (a) Transconductance component controlled by gate voltage, and (b) Additional transconductance component induced by impact ionization.
图7 基于峰分离法的直流跨导曲线分解结果 (a)受到栅压调控的跨导,以及(b)碰撞电离引起的额外跨导

probability, therefore in Fig. 8, if ignoring the impact-ionization probability, the linear relationship between the number of carriers entering the channel and V_{gs} will make transconductance curves similar to (a), and the V_{gs} corresponding to peak transconductance will not change. This systematic analysis confirms that the observed peak left-shifting exclusively originates from V_{dg}-enhanced ionization probabilities. Elevated ionization efficiency reduces the required carrier density for maximum transconductance, thereby shifting the peak toward lower V_{gs} values.

B Small-signal equivalent model

Mark Isler first introduces additional current sources in the small-signal model to account for the extra current resulting from impact ionization in the channel.

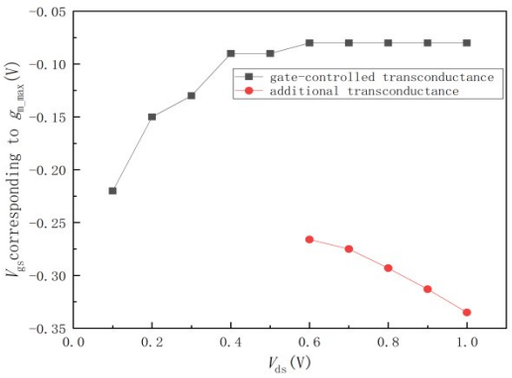

Fig. 8 Variation of V_{gs} corresponding to g_{m_max} with V_{ds}.
图8 最大跨导对应的Vgs随Vds的变化.

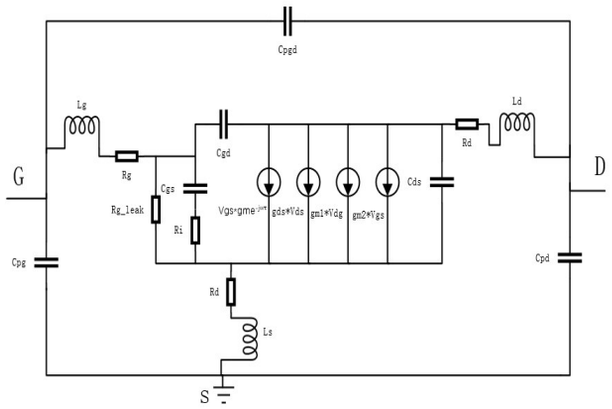

Fig. 9 Small-signal equivalent model.
图9 小信号等效模型

[13] On this basis, we would like to further explain the left shift phenomenon of transconductance curve when the impact ionization occurs.

From the measured S-parameters, a small-signal equivalent model is extracted, as shown in Fig. 9. The addition of two current sources can model the impact ionization effect for large applied drain biases in the devices, which leads to an increased output conductance due to both a direct increase in the drain electron current, as well as hole accumulation in the gate region. [14] Two current sources are controlled by V_{gs} and V_{dg} respectively, corresponding to the impact-ionization intensity affected by 2DEG and gate-drain electric field as mentioned earlier. Following the approach in [13], these effects are modeled using two frequency-dependent current sources described in (6) and (7):

$$g_{m1} = g_{m1,ii}/(1 + j\omega\tau_{ii}) \tag{6}$$

$$g_{m2} = g_{m2,ii}/(1 + j\omega\tau_{ii}) \tag{7}$$

In Equations (6) and (7), g_{m1} and g_{m2} are introduced to characterize the additional transconductance generated by impact ionization, while τ_{ii} represents the corresponding time constant.

The influence of impact ionization is mainly restricted to low frequencies, whereas at high frequencies, impact ionization effects are not able to follow the signal. [13] The introduction of the factor $1/(1+j\omega\tau_{ii})$ can reflect this frequency dependence. The value of τ_{ii} is generally between 10 ps and 100 ps, which means that when the frequency exceeds 10 GHz, the real part of g_{m1} (g_{m2}) will approach 0; when the frequency is below 1 GHz, the real part of g_{m1} (g_{m2}) is close to $g_{m1,ii}$ ($g_{m2,ii}$).

The extraction of small-signal model parameters is based on the theory of two-port networks, starting from extrinsic elements and gradually calculating towards intrinsic elements. The extrinsic element values, which exhibit bias-independence, are extracted first and summarized in Table 1. Subsequent derivation of intrinsic admittance (Y) parameters follows the methodology in [15]. Here, L_g, L_s, and L_d represent the parasitic inductances of the gate, source, and drain terminals, respectively, including contributions from metal feedlines and bonding pads. Similarly, R_g, R_s, and R_d correspond to the parasitic resistances of these terminals, accounting for ohmic losses in the metal interconnects and pad structures. The parasitic capacitances C_{pd} (drain pad-to-ground), C_{pg} (gate pad-to-ground), and C_{pgd} (gate-to-drain pad coupling) are also quantified in this model.

Table 1 Extrinsic elements of the composite channel HEMT
表1 复合沟道HEMT器件的外部寄生参数

Extrinsic elements		
C_{pg}=20 fF	L_g=40 pH	R_s=2 Ω
C_{pd}=29 fF	L_s=4.5 pH	R_d=4 Ω
C_{pgd}=9 fF	L_d=50 pH	R_g=13.8 Ω

Considering the proposed equivalent circuit model, the intrinsic Y-parameters of the HEMT are given by (8~11):

$$Y_{11} = j\omega C_{gd} + \frac{j\omega C_{gs}}{1 + j\omega C_{gs}R_i} + \frac{1}{R_{g\_leak}} \tag{8}$$

$$Y_{12} = -j\omega C_{gd} \tag{9}$$

$$Y_{21} = -j\omega C_{gd} + \frac{g_m e^{-j\omega\tau_{gs}}}{1 + j\omega C_{gs}R_i} + \frac{g_{m2,ii} - g_{m1,ii}}{1 + j\omega\tau_{ii}} \tag{10}$$

$$Y_{22} = j\omega(C_{gd} + C_{ds}) + g_{ds} + \frac{g_{m1,ii}}{1 + j\omega\tau_{ii}} \tag{11}$$

Intrinsic parameters have bias dependence, which can be used to study the impact of bias changes on transconductance. Here, C_{gs}, C_{ds}, and C_{gd} represent gate-source, drain-source, and gate-drain capacitances, respectively. g_m represents the transconductance, while τ_{gs} is the corresponding time constant. Besides, R_{g_leak} is introduced to characterize the gate-leakage current. Input resistance R_i governs channel charge control dynamics, while g_{ds} is the output conductance. C_{gd}, C_{gs}, R_i, and R_{g_leak} can be directly extracted by decomposing the real and imaginary parts of Y_{11} and Y_{12}. And as previously discussed, the frequency-dependent factor $1/(1+j\omega\tau_{ii})$

allows derivation of $g_{m1,ii}$ and g_{ds} through the following Equations:

$$\mathrm{real}(Y_{22}) = g_{ds}(f > 10\mathrm{GHz}) \quad (12)$$

$$\mathrm{real}(Y_{22}) = g_{ds} + g_{m1,ii}(f < 1\mathrm{GHz}) \quad (13)$$

By analyzing the imaginary parts of Y_{21} and Y_{22}, substituting the value of g_m, g_{ds}, $g_{m1,ii}$, and $g_{m2,ii}$, calculating and tuning the system of equations at multiple frequency points, the values of C_{ds}, τ_{gs} and τ_{ii} can be derived.

Fig. 10(a) and (b) show the changes in $g_{m1,ii}$ and $g_{m2,ii}$ caused by bias variation, respectively. g_{m1} and g_{m2} exhibit the same trend as DC characteristics: as V_{ds} gradually increases, V_{gs} corresponding to the maximum values of g_{m1} and g_{m2} gradually decreases.

Fig. 11 shows the variation of maximum g_m and corresponding V_{gs} with V_{ds} in the small-signal equivalent model, and its characteristics are consistent with the results of Fig. 7(a) and Fig. 8: g_{m_max} increases gradually with V_{ds} and approaches saturation when $V_{ds} \geqslant 0.6$ V; the V_{gs} corresponding to the maximum transconductance also gradually increases and stabilizes at high V_{ds} bias. Results illustrate that the small-signal model parameters are consistent with the peak splitting results: the left shift of the transconductance curve in DC measurement is caused by impact ionization, and the actual transconductance controlled by the gate still remains consistent with the curve of a conventional HEMT device.

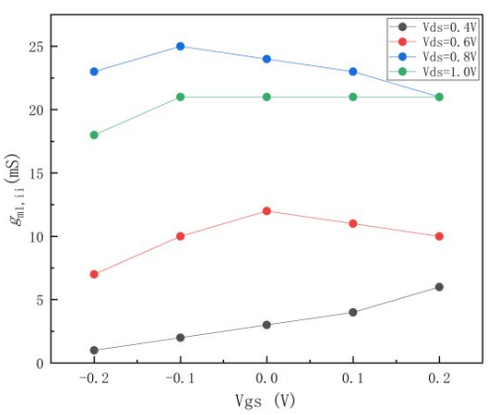

(a)

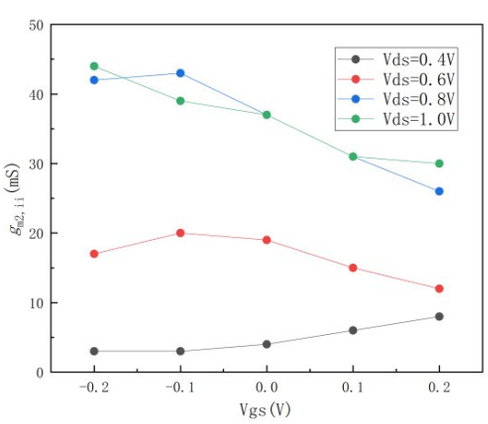

(b)

Fig. 10 Bias-dependent parameters of impact ionization-induced dual current sources in small-signal model. (a) $g_{m1,ii}$ versus V_{gs} under different V_{ds}, and (b) $g_{m2,ii}$ versus V_{gs} under different V_{ds}.
图 10 小信号模型中由碰撞电离诱导的双电流源参数的偏置依赖性分析(a) gm1,ii 在不同 Vds 条件下随 Vgs 的变化,以及(b) gm2,ii 在不同 Vds 条件下随 Vgs 的变化

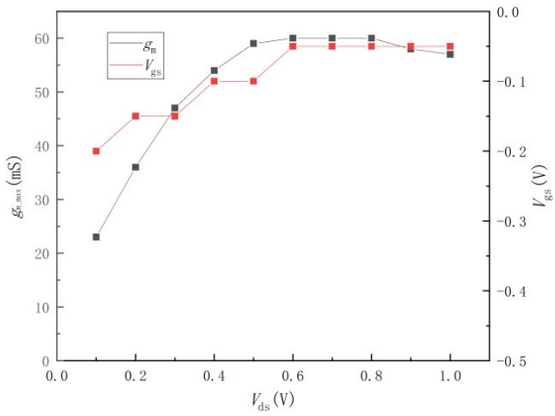

Fig. 11 The variation of g_{m_max} and corresponding V_{gs} with V_{ds}.
图 11 最大跨导及其对应 Vgs 随 Vds 的变化

An exception is observed in the results of Fig. 10: at $V_{ds} = 0.8$ V, the values of $g_{m2,ii}$ do not consistently exceed those at $V_{ds} = 1.0$ V, a phenomenon also reported in [13]. Nevertheless, these results still align with the physical mechanism of transconductance peak splitting observed in DC transfer characteristics — the V_{gs} corresponding to the maximum ionization-induced transconductance shifts leftward as V_{ds} increases. Additionally, the V_{gs} scanning step size of 0.1 V during testing confined the identified peak g_m values to integer grid points. This explains why Fig. 10(b) superficially suggests identical peak V_{gs} positions (−0.1 V) for both $V_{ds} = 0.6$ V and 0.8 V. Furthermore, while extrinsic parasitic parameters (e.g., R_s, R_d) are assumed bias-independent in small-signal modeling, actual parasitic resistances exhibit weak bias dependence. From a device physics perspective, bias variations alter ohmic contact properties and Schottky barrier resistance, introducing systematic errors in parameter extraction [11]. These factors collectively contribute to residual discrepancies in experimental results.

C RF characteristics

Table 2 shows the intrinsic parameters and frequency characteristics of the device when biased at $V_{gs} = -0.3$ V and $V_{ds} = 1$ V. The curve of U_g often exhibits fluctuations, which can easily cause significant errors when extrapolating f_{max}. To ensure accuracy, f_{max} and f_T are derived from the linear extrapolation of maximum available gain

(MAG) and maximum stable gain (MSG) curves, as shown in Fig. 12.

Table 2 the intrinsic parameters and RF characteristics of the composite channel HEMT
表2 复合沟道HEMT器件的本征参数和射频特性

C_{gs}(fF)	C_{gd}(fF)	C_{ds}(fF)	g_{ds}(mS)	g_m(mS)	$g_{m2,ii}$(mS)
27	5.5	3.5	3	50	35
$g_{m1,ii}$(mS)	τ_{ii}(ps)	τ_{gs}(ps)	f_T(GHz)	f_{max}(GHz)	$Ri(\Omega)$
15	34	<1	169	246	5

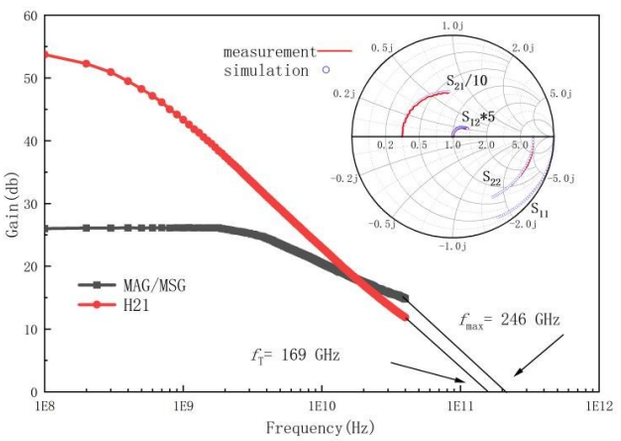

Fig. 12 Extrapolation of f_T and f_{max} from measured data and the fitting result of small-signal model compared with the measured S parameters.

图12 测试结果外推得到的f_T和f_{max}及小信号模型S参数拟合

A good fitting result of our small-signal model compared with the measured data is also shown in Fig. 12, which indicates the effectiveness and accuracy of our extracted parameters.

Fig. 13 shows the changes in RF characteristics of the device when the V_{ds} is increased from 0.1 V to 1 V with a step size of 0.1 V. The variation of f_T with V_{ds} is consistent with the trend of g_m with V_{ds} in Fig. 11, while f_{max} continues to rise with the increase of V_{ds}. The delay factor parameters in the small-signal model in Table II display $\tau_{ii} >> \tau_{gs}$, which indicates that impact-ionization effects are not able to follow the high frequency signal. In conventional InP-based HEMTs, the relationship between g_m and RF performance is shown in Equations (16) and (17)[16]:

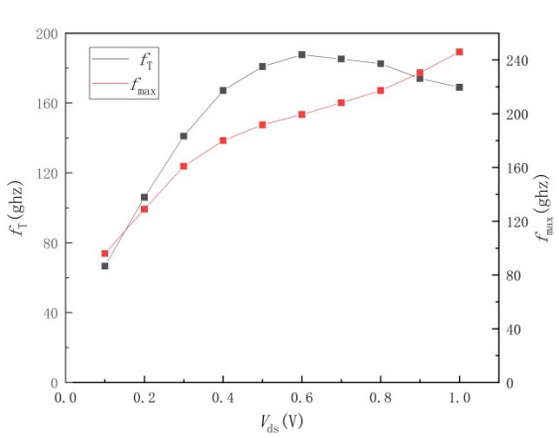

Fig. 13 RF characteristics at different V_{ds} bias.
图13 射频特性随Vds偏置不同的变化

$$f_T = \frac{g_m}{2\pi(C_{gs}+C_{gd})[1+g_{ds}(R_s+R_d)]+C_{gd}*g_m(R_s+R_d)} \quad (16)$$

$$f_{max} = \frac{f_T}{\sqrt{4g_{ds}(R_g+R_i+R_s)+2C_{gd}[C_{gd}/C_{gs}+g_m(R_i+R_s)]/C_{gs}}} \quad (17)$$

Based on the results of Figs. 11 and 12 with the positive correlation between f_T and g_m shown in (16), it is demonstrated that the actual gate-controlled g_m directly determines the RF characteristics. The continuous increase of f_{max} with V_{ds} is explained by (17): under high V_{ds} conditions, the output conductance g_{ds} decreases, thereby enhancing f_{max}.

The RF characteristics of this device are not as good as expected and lower than some reported devices in [4-6]. On the one hand, the results obtained by extrapolating f_{max} from MAG/MSG are relatively conservative. On the other hand, $\tau_{gs} << \tau_{ii}$, then as mentioned earlier, the value of g_m should be corrected to the actual gate-controlled g_m to eliminate the impact of impact ionization in our devices. This significantly reduces the RF performance of the device.

Table 3 shows some key performance parameters and fabrication strategies in some recently reported InP-based HEMTs.

g_m obtained by DC measurement can no longer intuitively reflect the RF characteristics, which brings greater difficulty and workload to the design and optimization of InAs channel HEMT devices. In order to control the strength of impact ionization, a gate offset in gate recess is an effective method that has been reported.[1] A gate closer to the source will increase the gate-drain distance, thereby reducing the actual gate-drain electric field to reduce the probability of carrier impact-ionization in the channel.

Compared to devices in [6] and [17], our device has a much longer L_g of 100 nm, and reducing the gate length can significantly improve g_m.

Consistent with the devices reported in Table 3, our design incorporates an InP etch-stop layer. However, this approach inadvertently increases the gate-to-channel distance (15 nm in our device vs. 9 nm in [5]), thereby degrading gate control efficiency. Reducing this distance to < 10 nm can enhance transconductance.

Reference [5] further highlights two common fabrication strategies for performance enhancement: asymmet-

ric gate recess and double-side delta doping. These techniques modify key parasitic parameters (like C_{gd}) in the small-signal model, thereby improving RF performance. Reference [6] and [18] report that increasing the length of gate recess leads to changes in parasitic capacitance and resistance, thereby resulting in lower f_T and higher f_{max}. However, a larger gate recess length often leads to an increase in surface states, and the kink effect will be more pronounced, especially for our device which retains the SiO_2 hard mask without passivation on the gate recess surface. Therefore, implementing such fabrication strategies requires careful consideration.

Reference [9] focuses on devices with SiO_2 hard masks similar to ours, analyzing the impact of hard mask removal on device performance. The study concludes that removing the hard mask enhances f_T but degrades f_{max}, suggesting that hard mask retention should be application-dependent.

As discussed in [17], adjusting the InAs layer thickness within the composite channel can enhance device performance. For our 10 nm composite-channel devices, the InAs layer thickness has already reached 5 nm, which is consistent with the maximum thickness reported in [18]. Therefore, the optimization priority for our device performance focuses on the above fabrication strategies.

3 Conclusion

In summary, we have fabricated a composite InGaAs/InAs/InGaAs channel HEMT and measured its DC and RF characteristics. The transconductance curve of the device exhibits a "left shift" anomaly. Through peak separation of the transconductance curves and analysis of the small-signal equivalent model, it is determined that this phenomenon is caused by impact ionization, resulting in additional transconductance which is not gate-controlled. This part of the transconductance has a "left shift" trend, and this shift is mainly due to changes in the electric field strength caused by changes in V_{dg}. The RF characteristics of the device further indicate that the additional transconductance caused by impact ionization cannot lead to higher f_T and f_{max}. Therefore, for InAs-channel devices prone to the kink effect, RF performance degradation should be mitigated by suppressing impact ionization, combined with a more accurate small-signal model to optimize device design.

Table 3 Performance Parameters and Fabrication Strategies of InP-Based HEMTs in Recent Literature
表3 近期文献中InP基HEMT器件的性能参数与制备策略

REF	L_g(nm)	Channel	g_{m_max}(mS/mm)	f_T(GHz)	f_{max}(GHz)	Features
[1]	100	$In_{0.53}Ga_{0.47}As$	1120	167	1096	Gate offset
[4]	87	$In_{0.8}Ga_{0.2}As$	3000	559	671	\
[5]	75	InAs	1331	260	800	Asymmetric gate recess 9nm distance between the gate and channel
[6]	20	$In_{0.8}Ga_{0.2}As$	3660	750	1100	Double-side-doped structure L_{side} variation
[9]	80	$In_{0.53}Ga_{0.47}As$	1087	304	524	SiO_2 hardmask etched
[18]	50	InAs	2100	392	678	InAs channel inset variation

References

[1] S. Cao, R. Feng, B. Wang, T. Liu, P. Ding, and Z. Jin, "Impact of gate offset in gate recess on DC and RF performance of InAlAs/InGaAs InP-based HEMTs," Chinese Physics B, vol. 31, p. 058502, 2022/06/01 2022, doi: 10.1088/1674-1056/ac464f.

[2] R. Lai, X. B. Mei, W. R. Deal, W. Yoshida, Y. M. Kim, P. H. Liu, J. Lee, J. Uyeda, V. Radisic, M. Lange, T. Gaier, L. Samoska, and A. Fung, "Sub 50 nm InP HEMT Device with Fmax Greater than 1 THz," presented at the 2007 IEEE International Electron Devices Meeting, Washington. DC, USA, Dec 10-12,2007, 2007.

[3] X. Mei, W. Yoshida, M. Lange, J. Lee, J. Zhou, P.-H. Liu, K. Leong, A. Zamora, J. Padilla, S. Sarkozy, R. Lai, and W. R. Deal, "First Demonstration of Amplification at 1 THz Using 25-nm InP High Electron Mobility Transistor Process," IEEEElectron Device Letters, vol. 36 4, pp. 327-329, 2015, doi: 10.1109/led. 2015. 2407193.

[4] H.-B. Jo, J.-M. Baek, D.-Y. Yun, S.-W. Son, J.-H. Lee, T.-W. Kim, D.-H. Kim, T. Tsutsumi, H. Sugiyama, and H. Matsuzaki, "Lg = 87 nm InAlAs/InGaAs High-electronmobility transistors with a gm_max of 3 S/mm and fT of 559 GHz," *IEEE Electron Device Letters*, vol. 39 pp. 1640-1643, 2018, doi: 10.1109/led.2018.2871221.

[5] M. Samnouni, N. Wichmann, X. Wallart, C. Coinon, S. Lepilliet, and S. Bollaert, "75 nm Gate Length PHEMT With fmax = 800 GHz Using Asymmetric Gate Recess: RF and Noise Investigation," *IEEE Transactions on Electron Devices*, vol. 68 pp. 4289-4295, 2021, doi: 10.1109/ted.2021.3098255.

[6] W. Park, H.-B. Jo, H.-J. Kim, S.-M. Choi, J. Yoo, J.-H. Kim, H.-S. Jeong, S. George, J.-M. Beak, I. Lee, T.-W. Kim, S.-K. Kim, J. Yun, T. E. Kim, T. Tsutsumi, H. Sugiyama, H. Matsuzaki, J. Lee, and D. Kim, "Terahertz In0.8 Ga0.2 As quantum-well HEMTs toward 6G applications," 2022 International Electron Devices Meeting (IEDM), 2022, doi: 10.1109/iedm45625.2022.10019567.

[7] C. Bolognesi, "Antimonide-based high-speed electronics: a transistor perspective," Conference Proceedings. 14th Indium Phosphide and Related Materials Conference (Cat. No. 02CH37307), 2002, doi: 10.1109/iciprm.2002.1014102.

[8] C.-Y. Chang, H.-T. Hsu, E. Y. Chang, C.-I. Kuo, S. Datta, M. Radosavljevic, Y. Miyamoto, and G.-W. Huang, "Investigation of Impact Ionization in InAs-Channel HEMT for High-Speed and Low-Power Applications," IEEE Electron Device Letters, vol. 28, pp. 856-858, 2007.

[9] F. G. Zhou, R. Z. Feng, S. R. Cao, Z. Y. Feng, T. Liu, Y. B. Su, J. Y. Shi, W. C. Din, and Z. Jin, "Impact of SiO2 hardmask on the DC and RF characteristics of InP HEMTs," *Journal of Materials Science:* Materials in Electronics, vol. 34, p. 2005, 2023/10/20 2023, doi: 10.1007/s10854-023-11404-8.

[10] H. Rodilla, J. Schleeh, P. Å. Nilsson, and J. V. Grahn, "Cryogenic Kink Effect in InP pHEMTs: A Pulsed Measurements Study," IEEE Transactions on Electron Devices, vol. 62, pp. 532-537, 2015.

[11] S. R. Cao, "Research on Gate Recess Structure of Terahertz InP HEMT for TMIC Applications," University of Chinese Academy of Sciences, Beijing, 2023.

[12] Y. H. Zhong, "Research on InP-based HEMT devices and Millimeter wave Monolithic Amplifier Circuits," 博士, Xidian University, Xian, 2013. [Online]. Available: https://kns.cnki.net/kcms2/article/abstract? v=sMQVub3UVPh8vhDfQGoypM0AJEcnNeY-auSZQGLFl5XvQzBqfH6Yvtp-q0PLi8E6ElxX3T3mQ_e8MFf8DThjqHgM-vEgq_EF9uC0GNj4HylNYEzjemi9O3epyy0anX1XKEwryJj-l3gQMEuicPdGuXDZaVPRgJMn9pyU9t-knvH3rbk3otys3NhK-kkvt5XkLKpYegGSNxYmU=&uniplatform=NZKPT&language=CHS

[13] M. Isler and K. Schunemann, "Impact-ionization effects on the high-frequency behavior of HFETs," IEEETransactions on Microwave Theory and Techniques, vol. 52 pp. 858-863, 2004, doi: 10.1109/tmtt.2004.823553.

[14] S. Johansson, M. Egard, S. G. Ghalamestani, B. M. Borg, M. Berg, L. E. Wernersson, and E. Lind, "RF Characterization of Vertical InAs Nanowire Wrap-Gate Transistors Integrated on Si Substrates," IEEE Transactions on Microwave Theory and Techniques, vol. 59, pp. 2733-2738, 2011.

[15] G. Dambrine, A. Cappy, F. Heliodore, and E. Playez, "A new method for determining the FET small-signal equivalent circuit," IEEETransactions on Microwave Theory and Techniques, vol. 36 pp. 1151-1159, 1988, doi: 10.1109/22.3650.

[16] P. J. Tasker and B. Hughes, "Importance of source and drain resistance to the maximum f/sub T/ of millimeter-wave MODFETs," IEEE Electron Device Letters, vol. 10, pp. 291-293, 1989, doi: 10.1109/55.29656.

[17] R. Z. Feng, W. Bo, S. R. Cao, L. Tong, Y. B. Su, W. C. Ding, P. Ding, and Z. Jin, "Impact of symmetric gate-recess length on the DC and RF characteristics of InP HEMTs," Chinese Phys. B, vol. 31, p. 018505, 2022/01/01 2022, doi: 10.1088/1674-1056/ac364d.

[18] D. C. Ruiz, T. Saranovac, D. Han, A. Hambitzer, and C. R. Bolognesi, "InAs Channel Inset Effects on the DC, RF, and Noise Properties of InP pHEMTs," IEEE Transactions on Electron Devices, vol. 99, pp. 1-7, 2019.